Efficient method for calculating Raman spectra of solids with impurities and alloys and its application to two-dimensional transition metal dichalcogenides

Arsalan Hashemi,[1] Arkady V. Krasheninnikov,[1,2] Martti Puska,[1] and Hannu-Pekka Komsa[1]
[1]*Department of Applied Physics, Aalto University, P.O. Box 11100, 00076 Aalto, Finland*
[2]*Helmholtz-Zentrum Dresden-Rossendorf, Institute of Ion Beam Physics and Materials Research, 01328 Dresden, Germany*

(Received 20 November 2018; published 28 February 2019)

Raman spectroscopy is a widely used, powerful, and nondestructive tool for studying the vibrational properties of bulk and low-dimensional materials. Raman spectra can be simulated using first-principles methods but due to the high computational cost calculations are usually limited only to fairly small unit cells, which makes it difficult to carry out simulations for alloys and defects. Here, we develop an efficient method for simulating Raman spectra of alloys, benchmark it against full density-functional theory calculations, and apply it to several alloys of two-dimensional (2D) transition metal dichalcogenides. In this method, the Raman tensor for the supercell mode is constructed by summing up the Raman tensors of the pristine system weighted by the projections of the supercell vibrational modes to those of the pristine system. This approach is not limited to 2D materials and should be applicable to any crystalline solid with defects and impurities. To efficiently evaluate vibrational modes of very large supercells, we adopt mass approximation, although it is limited to chemically and structurally similar atomic substitutions. To benchmark our method, we first apply it to the $Mo_xW_{(1-x)}S_2$ monolayer in the H phase where several experimental reports are available for comparison. Second, we consider $Mo_xW_{(1-x)}Te_2$ in the T′ phase, which has been proposed to be a 2D topological insulator but where experimental results for the monolayer alloy are still missing. We show that the projection scheme also provides a powerful tool for analyzing the origin of the alloy Raman-active modes in terms of the parent system eigenmodes. Finally, we examine the trends in characteristic Raman signatures for dilute concentrations of impurities in MoS_2.

DOI: 10.1103/PhysRevMaterials.3.023806

I. INTRODUCTION

Two-dimensional (2D) materials have been extensively studied for applications in optoelectronics, thermoelectrics, sensing, catalysis, etc. Although the catalog of available 2D materials is vast [1–3], it may be difficult to find a material that perfectly suits the desired specifications. In such cases, alloying can be used to further tune the material properties. Taking the transition metal dichalcogenide (TMD) family of 2D materials as an example, alloying the prototypical member MoS_2 with WS_2 or $MoSe_2$ leads to straightforward modification of electrical conductivity [4,5], band gap, band edges [6–11], and spin-orbit splitting [12]. More interestingly, alloying can even provide properties that were not present in the constituent phases. For instance, alloying can lead to dramatic reduction of the thermal conductivity [13,14] or passivation of defect levels [15,16]. The beneficial role of alloying has already been demonstrated in few applications: the response characteristics of $(Mo,W)S_2$-based photodetector [16] and the catalytic activities of $Mo(S,Se)_2$ alloys [17,18] were found to be better than in their parents.

Among TMD alloys, a particularly curious case is $(Mo,W)Te_2$ alloy since $MoTe_2$ is more stable in the H phase and WTe_2 is more stable in the T′ phase, although the energy differences between the two phases are small for both parent materials and, in fact, $MoTe_2$ can also be grown in the T′ phase. The phase tunability is particularly interesting for these materials as they have drastically different electronic properties in different phases. In the H phase, these materials are semiconductors, whereas in the T′ phase, they are semimetals or topological insulators depending on the number of layers [19–22]. Due to similar energies, coexistence of H/T phase regions has been predicted in Ref. [23], and it was also proposed that the H/T′ transition in $(Mo,W)Te_2$ could be promoted by gating [24]. Moreover, 2D ferroelectricity was recently demonstrated in T′-WTe_2 even in the monolayer limit [25].

Raman spectroscopy is an important and versatile tool for characterizing the composition of 2D alloys and assessing their overall crystal quality, but it is not always straightforward to assign new peaks (as compared to the spectrum of the parent systems) to the structural features from which they originate from. Several TMD alloys have already been extensively studied in the literature by Raman spectroscopy providing datasets covering a full composition range in many alloy systems, such as $(Mo,W)S_2$ [26–28] $(Mo,W)Se_2$ [29,30] $Mo(S,Se)_2$ [9,10,31,32] $Re(S,Se)_2$ [33]. For bulk alloys, similar studies are also performed [34] and for T′-$(Mo,W)Te_2$ we are only aware of bulk alloy studies [35,36] but not of monolayer alloys.

There also exists a lot of computational studies for the Raman spectra for pristine, constituent phases [37–39], and even few reports for defective MoS_2 [40,41]. Despite the importance of Raman spectroscopy in understanding the alloy composition and the structural order, computational studies for alloys are missing. The reason is that, within the conventional computational approach, these calculations are computationally significantly more challenging due to the larger supercells (SCs) involved and the dramatic scaling of the

computational cost with the supercell size. When the maximum computationally feasible supercells sizes are often 3×3 or at maximum 6×6 primitive cells (PCs) it is clear that: (i) the impurity/defect concentration is necessarily high, and (ii) the defects are ordered, and thus the simulated spectra for a given alloy are unlikely to correctly mimic that of the randomly distributed system. These issues need to be tackled before computational Raman spectra for alloys can be calculated in a way that can be reliably compared to experiments and even holds predictive power.

In this paper, we propose a computational method to simulate Raman spectra of alloys using large supercells. The method relies on the projection of the vibrational eigenvectors of the supercell to those of the primitive cell, which are then used to weight the Raman tensors of the pristine system. When the lattice constants and the bonding chemistry in the two components are similar as is the case in the systems considered here, the supercell eigenvectors can be efficiently solved using the mass approximation (MA). We benchmark our method both towards the full density functional theory (DFT) approach in small supercells as well as experimental results. We first apply our method with the $(Mo,W)S_2$ alloy, for which extensive experimental results are available. We analyze the modes and, in particular, try to distinguish between the one-mode and two-mode behaviors, and visualize the eigenmodes that contribute to the most prominent Raman peaks. Next, we consider T′-phase $(Mo,W)Te_2$, which is much more involved due to the lower symmetry, larger supercell, and (semi-)metallic electronic structure, whereas a mass approximation is expected to hold equally well. Finally, we consider dilute concentrations of impurities in MoS_2, both in the Mo site and in the chalcogen site, and look for characteristic Raman signatures.

II. METHODS

A. Theoretical framework

As mentioned in the Introduction, first-principles Raman calculations for large unit cells are computationally challenging. They involve two steps: (i) determination of the vibrational modes of the system and (ii) calculation of the Raman activity for each mode.

In step (i), the vibrational modes (eigenmodes) are solutions to

$$M_k\omega^2\mathbf{v}(k0) = \sum_{k',l} \Phi(k'l,k0)\mathbf{v}(k'l) \quad (1)$$

$$= \sum_{k',l} \Phi(k'l,k0)\exp(-i\mathbf{q}\cdot\mathbf{R}_l)\mathbf{v}(k'0), \quad (2)$$

where $\mathbf{v}(kl)$ are the eigenvectors for the displacement of atom k with mass M_k located in cell l specified by the lattice vector $\mathbf{R}_l$. The elements of force constant (FC) matrix Φ are defined by the change in potential-energy U with respect to the atomic displacements,

$$\Phi_{\alpha\beta}(k'l,k0) = \frac{\partial^2 U}{\partial u_\alpha(k'l)\partial u_\beta(k0)}.$$

Above, $u_\alpha(kl)$ denotes the displacement of the kth atom in the lth unit cell in the Cartesian direction α. Constructing the force constant matrix in the case of alloys, without any symmetry, essentially requires performing $3N$ DFT total energy calculations in which each of the N atoms is displaced in each of the three Cartesian directions.

In step (ii), the Raman intensity can be written as

$$I \sim |\mathbf{e}_s \cdot R \cdot \mathbf{e}_i|^2, \quad (3)$$

where $\mathbf{e}_i$ and $\mathbf{e}_s$ denote the polarization vectors of the incident and scattered light and R is the Raman tensor. In the case of nonresonant first-order Raman scattering, it is obtained from the change in polarizability χ with respect to the phonon eigenvectors $\mathbf{v}$, and in first-principles calculations it can be evaluated by using the macroscopic dielectric constant ε_{mac} as

$$R \sim \frac{\partial\chi}{\partial\mathbf{v}} = \frac{\partial\varepsilon_{\text{mac}}}{\partial\mathbf{v}}. \quad (4)$$

This derivative needs to be evaluated at both the positive and the negative displacements for each of the $3N$ eigenvectors $\mathbf{v}$, yielding a total of $6N$ calculations. Moreover, despite different approaches, evaluating ε_{mac} is generally significantly more time consuming than DFT total energy calculations.

Although step (ii) takes more time, already step (i) becomes challenging in large low-symmetry systems. In the case of MoS_2, the limitations are currently at around a 10×10 supercell for step (i) and a 6×6 supercell for step (ii). In order to properly account for the random distribution of atoms and the resulting broadening of the spectra, large supercells or averaging over several configurations is required. Herein, we adopt two approximations to tackle each of these issues: a mass approximation for step (i) and projection to the primitive cell Raman-active eigenmodes for step (ii).

In the MA, only masses are changed in Eq. (1), whereas the force-constant matrix remains untouched [42,43]. Naturally, this can only be applied in cases where the nature of the bonding and the atomic structure remain very similar, such as, for instance, $Al_xGa_{1-x}As$ [42].

Due to the small momentum of photons commonly used in Raman spectroscopy and especially in nonresonant Raman where the photon energy needs to be less than the band gap, first-order Raman scattering can only involve a single phonon near $q = 0$. For pristine materials, the $q = 0$ phonons are trivially obtained as the Γ-point solutions of Eq. (1) in the PC. If we consider a SC of pristine material, the Γ-point contains several modes from the folding of the phonon bands. In an explicit calculation of Raman intensities using Eq. (4), the intensities of the folded modes will be zero, and thus the Raman spectra remains the same. Alternatively, the folded modes in the supercell Γ point could be unfolded back to the primitive cell Brillouin zone (BZ) through projection to plane waves $g(\mathbf{q}) = \exp(i\mathbf{q}\cdot\mathbf{R})$, where $\mathbf{q}$ corresponds to one of the PC q points that fold into the Γ point of the SC. Adopting the notation where $\mathbf{v}^{\text{SC}}(kl)$ refers to the lth primitive cell within the supercell and k indexes the atoms in the unit cell, the projection is written out as

$$\langle g(\mathbf{q})|\mathbf{v}^{\text{SC}}\rangle_{\alpha,k} = \sum_l \exp(-i\mathbf{q}\cdot\mathbf{R}_l)v_\alpha^{\text{SC}}(kl). \quad (5)$$

Although we could use this equation to unfold to any $\mathbf{q}$, we are here primarily interested in the Γ point, which fortuitously also yields a particularly simple expression since the exponent in Eq. (5) is always unity, and thus one ends up with a

straightforward sum over the eigenvectors. The total Γ-point weight can be obtained by taking the square of the projections and summing up over k and α. Finally, we sum up over all the SC states i with frequency ω_i to obtain Γ-point weighted density of states,

$$n(\omega) = \sum_i \sum_{\alpha,k} |\langle g(\mathbf{q})|\mathbf{v}^{\mathrm{SC},i}\rangle_{\alpha,k}|^2 \delta(\omega - \omega_i) \tag{6}$$

which we here denote as GDOS. Since each mode in pristine supercell has nonzero weight in only a single q point in the PC BZ, the true $q = 0$ modes can easily be found. In alloys or defective systems where the translational symmetry is broken, the unfolding/projection procedure still works but leads to each SC mode having contributions from q points throughout the PC BZ with different weights. This type of unfolding procedure has already been used in the past to analyze both the electronic and the phonon band structures of alloys [44–47].

Baroni *et al.* found that the GDOS of the primitive cell can be used to closely approximate the Raman spectra [42] in alloys. The modes which were inactive due to momentum-conservation law can gain weight at $q = 0$ and start to show up in the Raman spectra and, vice versa, the modes that were originally purely $q = 0$ modes can leak weight to other q points and thereby lose Raman intensity. Such an analysis is straightforward when the frequencies of Raman-active and Raman-inactive modes are clearly separated. If they are close, it is no longer clear which part of the GDOS would be Raman active. To solve this issue, we here propose to project the SC modes not to plane waves but to PC eigenmodes at the Γ point. That is, adopting the same notation for $\mathbf{v}^{\mathrm{SC}}(kl)$ as above,

$$w_{ij} = \langle \mathbf{v}^{\mathrm{PC},i}|\mathbf{v}^{\mathrm{SC},j}\rangle = \sum_{\alpha,k,l} v_\alpha^{\mathrm{PC},i}(k0) v_\alpha^{\mathrm{SC},j}(kl). \tag{7}$$

Here, due to the mass approximation, the atoms are in the same positions both in the alloy and in the pristine cells. However, it appears to work well also with the DFT relaxed structures. Since the projection is to PC modes at the Γ point, we simultaneously obtain the Γ-point projection (or unfolding). We note that the summation of projections w_{ij}^2 over all k and α yields the same GDOS as via the plane-wave projections [Eq. (6)] since both constitute a complete basis set. The Raman tensor of the SC mode is obtained by multiplying the PC mode projection by the respective Raman tensors from the pristine system, i.e.,

$$R^{\mathrm{SC},j} = \sum_i w_{ij} R^{\mathrm{PC},i}, \tag{8}$$

where the sum goes over PC modes i and clearly only Raman-active modes contribute. Finally, the Raman intensity of the SC mode j is obtained using Eq. (3), which yields

$$I^{\mathrm{SC},j} \sim |\mathbf{e}_s \cdot R^{\mathrm{SC},j} \cdot \mathbf{e}_i|^2 \tag{9}$$

$$= \sum_i w_{ij}^2 |\mathbf{e}_s \cdot R^{\mathrm{PC},i} \cdot \mathbf{e}_i|^2 + \sum_{i\neq k} (\mathbf{e}_s \cdot w_{ij} R^{\mathrm{PC},i} \cdot \mathbf{e}_i)^* (\mathbf{e}_s \cdot w_{kj} R^{\mathrm{PC},k} \cdot \mathbf{e}_i) \tag{10}$$

$$\approx \sum_i w_{ij}^2 I^{\mathrm{PC},i}. \tag{11}$$

Squaring the sum over PC modes leads to $i = k$ and $i \neq k$ terms, which have been separated in the second step. These cross terms can be important if the SC mode has appreciable weight arising from several PC modes. In the last step, we have assumed that they are negligible. Although, indeed, not always a good assumption, the advantage is that we can now sum over intensities rather than Raman tensors. This is useful because we could then, e.g., use experimentally determined intensities instead of the calculated ones. We denote the total Raman intensity-weighted GDOS as RGDOS. When the contributions from each mode to the total Raman spectra are shown in the Results section, these correspond only to the first term in Eq. (10). We note that in some previous works the Raman tensor in alloy/defective supercells has been decomposed using the Raman tensors of different symmetries of the pristine host for the analysis purposes [48,49]. Here, we essentially proceed in the opposite direction in order to construct the final Raman tensor. Moreover, our approach is, in principle, more general as it can distinguish between different modes of the same symmetry.

To sum up, the main ingredients of the method lie in the projection of the supercell vibrational eigenmodes to the pristine system eigenmodes [Eq. (7)] and using those projections as weights when summing up over the primitive cell Raman tensors [Eq. (8)]. The general applicability of our method is mostly limited by the eigenmode projection, which essentially requires that there needs to be a reasonable mapping between the atomic structures of the nonpristine and pristine systems. Extension of the method to simulate second-order nonresonant scattering should be fairly straightforward. To simulate resonant Raman scattering, in principle, one can just plug the resonant Raman tensors into Eq. (8). In practice, the modifications of the electronic structure need to be also carefully considered, the details of which strongly depend on the system.

B. Computational details and benchmarking

All first-principles calculations are carried out with VASP [50]. Exchange-correlation contributions are treated with the PBEsol functional [51]. A plane-wave basis with a cutoff energy of 550 eV is employed to represent the electronic wave functions. The geometry optimization continues until the energy differences and ionic forces are converged to less than 10^{-6} eV and 1 meV/Å, respectively. The first Brillouin zone of the primitive cell is sampled by a 12×12 mesh for H-MoS_2/WS_2 and by a 12×24 mesh for T′-$MoTe_2$/WTe_2 and changing in proportion to the supercell size. The polarizability tensors for Raman calculations are determined within the framework of the finite displacement method [52]. The phonon spectra are assessed using the PHONOPY code [53] using a 6×6 supercell for MoS_2/WS_2 and a 4×4 supercell for $MoTe_2$/WTe_2. The Raman intensity is calculated as an average over the XX and XY configurations for the light polarization ($\mathbf{e}_i\mathbf{e}_s$).

We start by benchmarking our computational scheme with respect to the mass approximation. We show in Fig. 1(a) the phonon dispersion curves of MoS_2 and WS_2 calculated with DFT and the mass-approximated versions (i.e., using the MoS_2 FC matrix but substituting the mass of Mo by that of

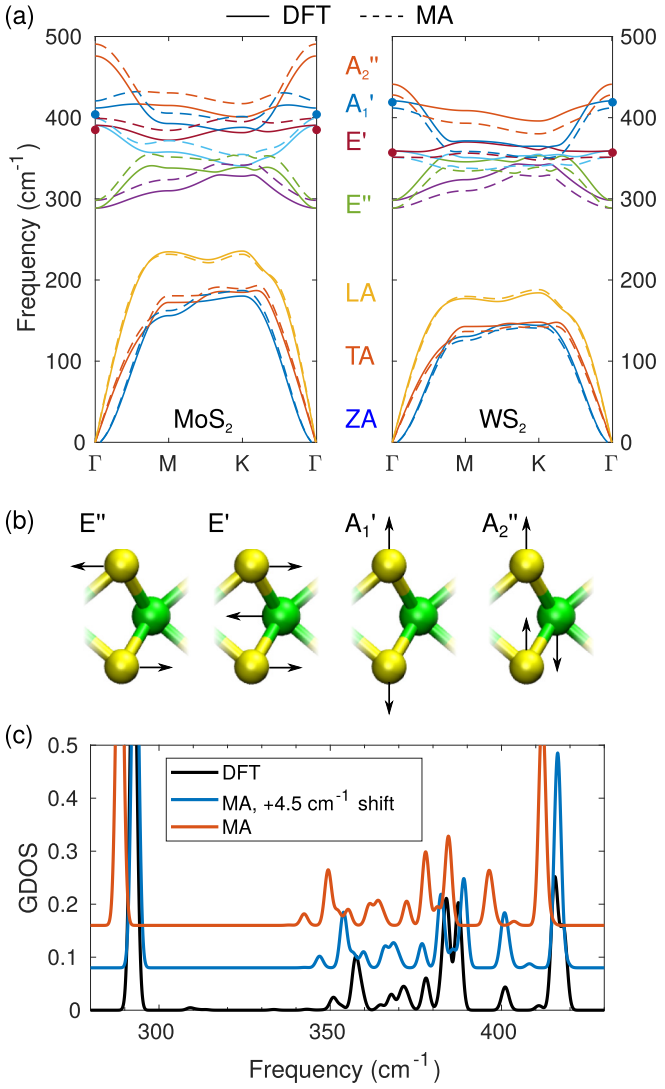

FIG. 1. (a) Phonon dispersion curves of pristine MoS_2 (left) and WS_2 (right) calculated either self-consistently using DFT (solid lines) or using the mass approximation (dashed lines). Dots denote experimental values obtained from Raman spectroscopy [38,54]. (b) Schematic illustration showing the vibrations of Mo (green) and S (yellow) atoms in different optical phonon modes. (c) GDOS from 3×3 special quasirandom structures (SQSs) of $Mo_{0.56}W_{0.44}S_2$, either calculated fully with DFT or using the mass approximation.

W and vice versa). The dispersions of the bands are captured very well with MA as are the acoustic mode frequencies. There is a nearly constant downshift of the optical mode frequencies of WS_2 by about 10 cm^{-1} with respect to the self-consistent WS_2 calculation, and vice versa an upshift in MoS_2 frequencies if using WS_2 FC with the Mo mass, suggesting that W-S bonds are slightly stronger than Mo-S bonds. In the following of this paper, we have chosen to use the MoS_2 force constants. With this choice, when comparing to the experimental values for the two Raman-active modes, E' and A_1', our calculated frequencies are slightly overestimated for MoS_2 and slightly underestimated for WS_2 when compared to full DFT calculation.

The effect of MA is further illustrated in Fig. 1(c) in the case of the (Mo,W)S_2 alloy supercell. The structural models used in the alloy calculations are constructed using the SQS method [55]. As seen in Fig. 1(c) for 3×3 $Mo_{0.56}W_{0.44}S_2$ SQS, the MA frequencies are downshifted throughout the spectrum, similar to the pristine systems. To allow for a better comparison with the DFT results, we also show a spectrum shifted up by 4.5 cm^{-1} (from the alloy composition times 10 cm^{-1}), after which the main peaks (E', A_1') and the high-frequency part of the E' feature (from 350 to 400 cm^{-1}) agree very well. The low-frequency part of the E'' features has still a too low frequency, which is due to the fact that these modes are localized to W atoms as will be seen later.

Next, we inspect the importance of statistical sampling. We use the supercell comprising 12×12 primitive cells and 20 different random configurations (not SQS) for each composition. Figure 2(a) shows the spectra from all the 20 configurations and the averaged spectra. The large variation in the single spectra indicates that 12×12 supercell is still not quite large enough to correctly describe the alloy with a single supercell. As shown in the inset, averaging over just four configurations yields a spectrum that is already quite similar to that from 20 configurations. In addition, we compare the averaged spectrum to that of a SQS model created within the 12×12 supercell. We consider pairs up to 8 Å [three effective cluster interaction (ECI) parameters] and three-body clusters up to 4 Å (two ECI). The SQS performs better than the different random configurations but fails to correctly capture the smooth broadening of the main peaks, instead yielding more spiked features. This originates from the coarseness of the mesh of k points that folds into the Γ point in small supercell calculations. Note, that the A_1' mode is, in practice, completely unaffected by the mixing as it only involves movement of the chalcogen atoms and the metal atoms are fixed [see Fig. 1(b)].

Finally, we benchmark the eigenmode-projection scheme. First, we illustrate in Fig. 2(b) the eigenmode contributions in the case of 12×12 SQS. In the H-(Mo,W)S_2 alloy, the modes remain fairly separated in frequency, and thus, the resulting Raman spectra could be fairly safely evaluated from just the GDOS. On the other hand, the projection scheme provides further insight into the origin of the spectral features. For instance, the bump at around 400 cm^{-1} originates from the E' mode and not from the A_1' mode. Also, at large W concentration, the A_2'' features start to overlap with the E'/A_1' features as will be seen in the Results section. Moreover, we need to compare how well the approximated Raman spectra match to explicit Raman calculations. For this, we need to adopt a smaller system, and since this is only for benchmarking purposes, we can take a 3×3 supercell, again created using the SQS scheme. The RGDOS captures surprisingly well all the features of the full Raman calculation as shown in Fig. 2(c). Especially, the peak shapes/structures are correctly reproduced, even if some intensities differ with the most significant discrepancy occuring near 385 cm^{-1}. From the comparison of the spectra in Figs. 2(b) and 2(c), it is again obvious that 3×3 SQS cannot describe properly the Raman spectrum of the random alloy.

We have demonstrated that large supercells are needed to properly describe the phonon spectra of random alloys

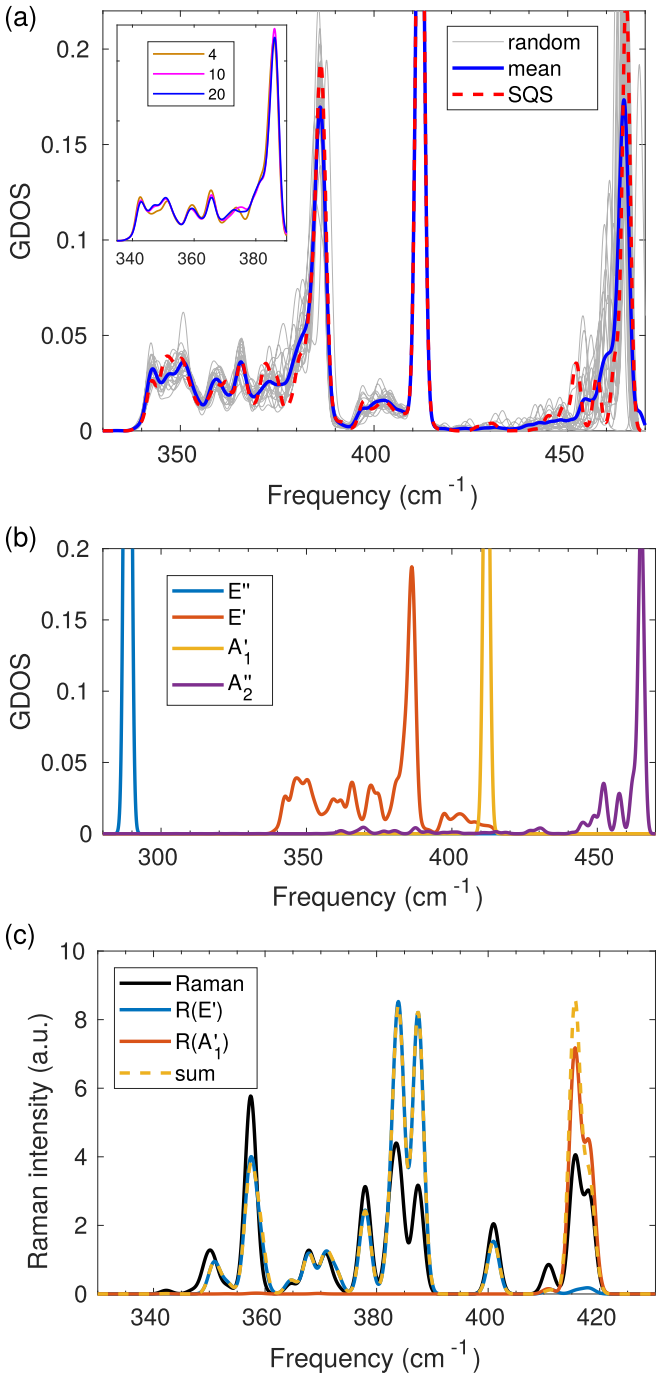

FIG. 2. (a) GDOS from 20 random atomic configurations for $Mo_{0.56}W_{0.44}S_2$ (gray lines) together with their average (blue, solid line). GDOS for the 12×12 SQS supercell is also shown for comparison. The inset: Comparison of results when the averaging is performed over 4, 10, or 20 configurations. (b) Primitive cell eigenmode projected GDOS for the SQS cell [the same as in panel (a)]. (c) Raman spectra from full DFT calculation for the 3×3 SQS supercell of $Mo_{0.56}W_{0.44}S_2$ compared to its RGDOS and the contributions to it from the two primitive cell eigenmodes.

and that RGDOS can be used to give a good estimate of the Raman spectrum. Although the mass approximation may produce some inaccuracies with the peak positions, we feel that this is acceptable trade-off for the ability to correctly describe the random alloy. In the following, the results for the alloys are obtained by averaging over 20 configurations of the 12×12 supercell and using the eigenmode projection. In a few cases, the analysis of the results is performed using the SQS structure, which results in great simplification.

III. RESULTS

A. H-(Mo,W)S_2

The simulated Raman spectra for the H-(Mo,W)S_2 monolayer as a function of the composition are shown in Fig. 3(a), and which can be compared to experimental Raman spectra shown in Fig. 3(b) (from Ref. [26]). The calculated A_2'' mode, although not Raman active, is also shown, since it is infrared active and shows large changes with the composition. To make it visible in the simulated spectra we use the same Raman tensor as for A_1'. The experimental and calculated peak positions are collected in Fig. 3(c). The A_1' mode consists of only the chalcogen movement, and thus, in our mass-approximation approach this mode remains strictly constant. Also E'' is unaffected by the MA and, thus, not shown in the calculated spectra, although its activation due to disorder is visible in the experimental spectra.

Overall a good agreement with the experiment is observed for the number of peaks as well as their positions: (i) For the E' mode, we confirm pronounced two-mode behavior with the separate MoS_2- and WS_2-derived peaks. (ii) There is a clear downshift of the $E'(MoS_2)$ peak, whereas the $E'(WS_2)$ peak remains nearly constant in energy. In experiment, at the large W concentration, the MoS_2-derived peak broadens and possibly mixes with the d feature (marked d as it was denoted the "disorder-related mode" in Ref. [26]). (iii) There are two additional features around the WS_2 peak: one at about 345 cm^{-1} (marked #) and one at about 360 cm^{-1} (unmarked) in calculations. The latter is difficult to observe in Fig. 3(b) but evident in the line shape fits in Ref. [26]. (iv) Both in experiment and theory, at small W concentrations, the W-derived features form a broad plateau below the $E'(MoS_2)$ peak with no particularly distinct peaks. (v) A small bump develops between the $E'(MoS_2)$ and A_1' peaks, which originates fully from the E' mode. Whereas in calculations, it prevails at intermediate concentrations, in experiments this is only clearly visible at the W-rich side, and thus it is not clear if their origin is the same.

In order to understand the atomic origin of these peaks, we illustrate the eigenvectors from selected cases in Fig. 3(d) where the sizes of the circles at the position of atom k correspond to the eigenvector weighted by the Γ-point projection $|\mathbf{v}(k0)|^2 \cdot w^2$ summed over all modes within the selected range of frequencies marked in Fig. 3(a). As expected, the modes corresponding to MoS_2- and WS_2-derived peaks are localized around Mo and W atoms, respectively. The broader feature between E' and A_1' appears to be localized at the edges of the Mo regions [panel (iii)]. The disorder-related mode is not very visible at $x = 0.5$, but at $x = 0.875$, our analysis clearly shows that it is localized to isolated Mo atoms [panel (iv)].

The smaller peaks around it, on the other hand, are localized to Mo clusters (not shown), whose density at W-rich samples is naturally small. Eigenmodes for the peaks

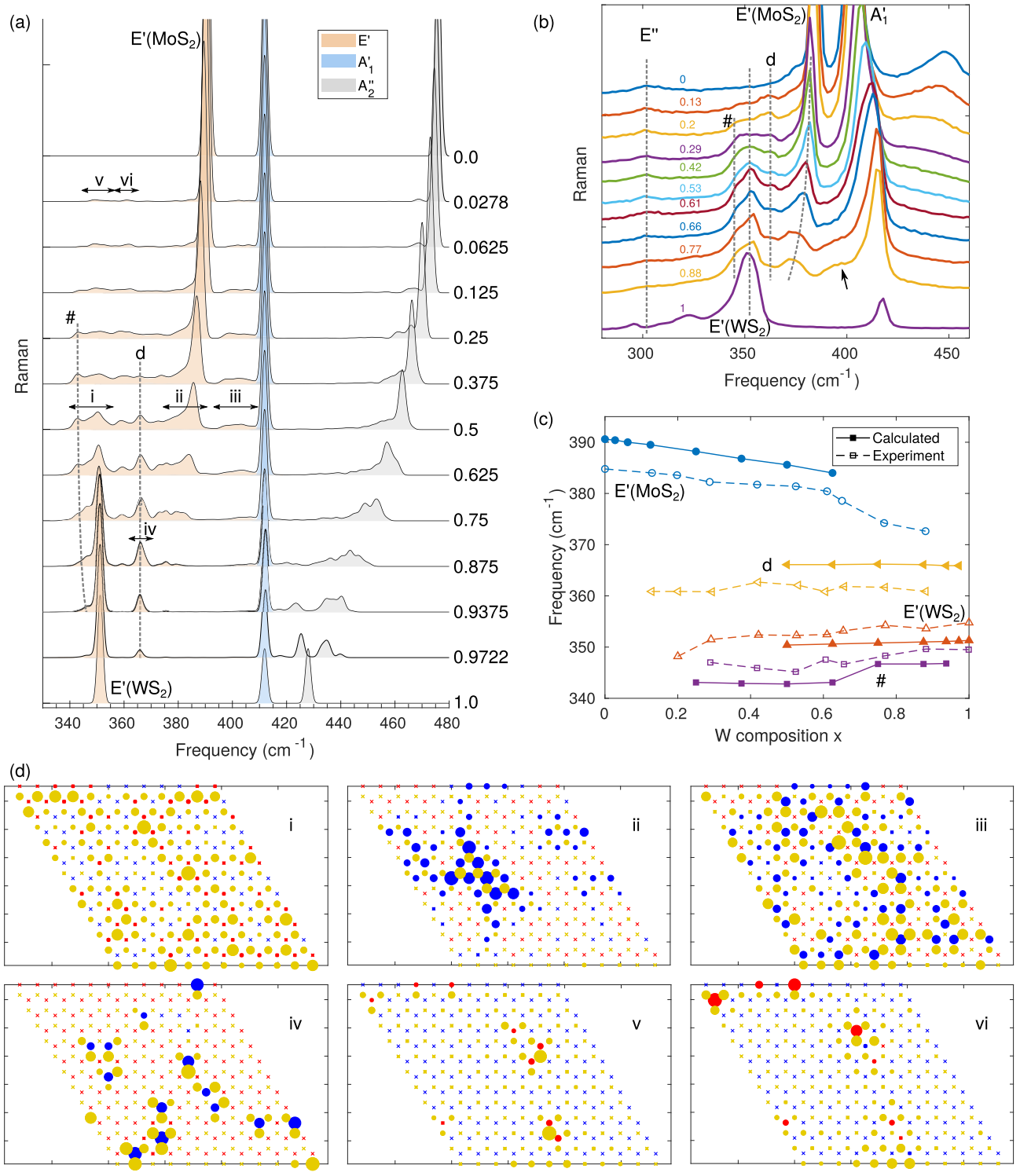

FIG. 3. (a) RGDOS for the $Mo_{1-x}W_xS_2$ alloy x ranges from 0 to 1. The total RGDOS is shown with the solid black line. The contributions from E', A_1', and A_2'' modes are shown by yellow, blue, and gray shaded areas, repectively. (b) Experiments, adapted from Ref. [26]. (c) The calculated compositional dependence of the Raman peaks frequencies vs the experimental counterparts. (d) Illustration of selected eigenmodes (i–iv) from (a). The blue, red, and yellow symbols correspond to Mo, W, and S atoms, respectively, and the magnitude of symbols is proportional to the amplitude of vibrations.

denoted by # appear visually very similar to the main WS_2-derived modes, and thus, we think that this shoulder just originates from asymmetrical broadening of the WS_2 peak. On the other hand, this peak was assigned to a combination of two longitudinal acoustic modes [2LA(M)] in Ref. [26]. Our calculated LA(M) frequency for WS_2 is 177 cm^{-1}, yielding 2LA(M) at 354 cm^{-1} and, thus, lies slightly above the $E'(WS_2)$ peak in our calculations but could also be slightly

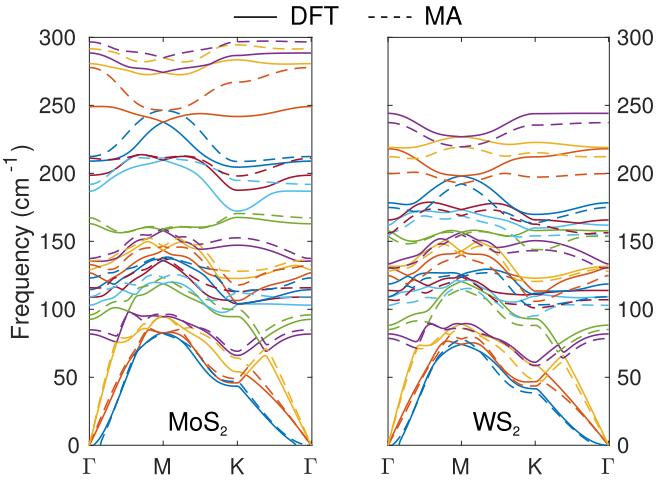

FIG. 4. Phonon dispersion curves of pristine $MoTe_2$ (left) and WTe_2 (right) calculated either self-consistently using DFT (solid lines) or using mass approximation (dashed lines).

below the $E'(WS_2)$ peak in experiments. Since we here only simulate the first-order Raman scattering, we know that the shoulder in calculations contains no 2LA(M) contribution, but naturally we cannot exclude such additional contributions in the experimental spectra.

B. T′-(Mo,W)Te$_2$

We next study T′-(Mo,W)Te_2 alloy, which is computationally a significantly more challenging case since (i) the unit cell is larger and has lower symmetry than the H phase, thus leading to larger number of displacements in pristine system, and (ii) it is (semi-)metallic, necessitating the use of large k-point meshes. The latter also means that the Raman spectra will necessarily be resonant, but the evaluation of the Raman tensor from the change of macroscopic dielectric constant assumes nonresonant conditions. Resonant Raman tensors can be used just as well in our approach for simulated Raman spectra [Eq. (9)], but their evaluation from first principles is again step up in computational complexity and, moreover, makes the tensors frequency dependent. To avoid these problems, we here use the nonresonant Raman tensors, which are moreover normalized in order to better highlight all the Raman-active features, although this means that the relative intensities of the peaks are not correctly captured. The classification of the Γ-point vibrations $\Gamma_{C_i} = 9A_g + 9A_u$ shows that half (A_g) of the modes are Raman active. These modes can be arranged in two groups: modes vibrating along the direction of the zigzag Mo/W chain, denoted by A_g^z, and modes vibrating perpendicular to the zigzag chain, denoted by A_g^a.

Phonon dispersion curves calculated by DFT and by mass approximation are shown in Fig. 4. We again observe that frequencies from MA are shifted down by about 10 cm^{-1} in WTe_2, but the order and dispersion of the bands are captured well. The only clear deviation occurs for WTe_2 around 220 cm^{-1} at the Γ point, where the quasidegenerate Raman active modes from the DFT calculation breaks into two modes at 200 and 212 cm^{-1} from the MA calculation, echoing the splitting observed in $MoTe_2$ at 250 and 280 cm^{-1}. This feature is observed in experiment for bulk (Mo,W)Te_2 [56]. It is worth noting that the lattice constants of $MoTe_2$ (3.37 and 7.15 Å) and WTe_2 (3.42 and 7.12 Å) are not quite as close as those of the parent compounds in H-(Mo,W)S_2.

The calculated RGDOS for the monolayer T′-(Mo,W)Te_2 alloy as a function of composition are shown in Fig. 5(a) and the peak positions are collected in Fig. 5(b). We recall, that although in H-(Mo,W)S_2 the alloy modes could be easily assigned to the pristine modes from which they originated thanks to the large separation in frequency, here due to the large number of modes, the mixing is more complicated and thus the eigenmode projection is necessary to distinguish between the Raman-active and Raman-inactive features. The projection scheme allows us to distinguish the origins of each peak in terms of the primitive cell eigenmodes, revealing that the ordering of the modes is retained in the same order throughout the alloys. The eigenvectors of these modes in the parent phases have been illustrated in several previous works [57–64] and are not repeated here. Nevertheless, they show that the six lowest frequency modes are mostly localized to Te atoms, and the three high-frequency modes to Mo/W atoms. Consequently, the six lowest-frequency modes exhibit single-mode behavior, and the three high-frequency modes two-mode behavior, reflecting the fact that alloying is carried out in the metal sublattice. Among the six lowest-frequency modes that exhibit the single-mode behavior, the third one is silent in the metal sublattice, and the fifth one nearly silent [58], and thus they show very little changes upon alloying. There are also clear differences in the degree of the alloying-induced broadening of the other four peaks with the first one showing the least broadening, the second one showing the strongest broadening, and the fourth and sixth modes falling in between. Figure 5(c) illustrates the second and fourth modes of the $x = 0.75$ alloy. The fourth mode [panel (ii)] is localized very clearly only on the Te atoms and mostly on the rows with long metal-metal distance, whereas the second mode has also weight on the metal atoms and is mostly localized on the rows with short metal-metal distance.

The last three modes in Fig. 5(a) show a very clear two-mode behavior with splitting into $MoTe_2$- and WTe_2-like modes at intermediate alloy concentrations. The eigenvectors in Fig. 5(c) show that these modes are localized almost completely on the metal atoms and the two-mode behavior reflects the localization around Mo and W atoms. The eigenmode projections illustrated in Fig. 5(c) are found to provide additional insight into the peak origins. For instance, there is a mode at 200 cm^{-1} in both the $MoTe_2$ and the WTe_2 phases, but the projections reveal that they correspond to different modes. Somewhat similarly, the 160 cm^{-1} peak in WTe_2 is seen to contain two modes, which in the $MoTe_2$ region are located at 160 cm^{-1} and 200 cm^{-1}.

Comparison to experimental results is hindered by the fact, that to the best of our knowledge, all the experimental T′-$Mo_{(1-x)}W_xTe_2$ alloy results are from bulk samples [4,35,36,65]. Monolayer data are only available for pure $MoTe_2$ and WTe_2 [57–59]. Naturally, there exists also a large body of data for pure bulk or few-layer phases [56,60–64,66]. Although the bulk and monolayer frequencies are generally fairly close, to facilitate a proper comparison, in Fig. 5(b) we only show the available monolayer results for $MoTe_2$ and

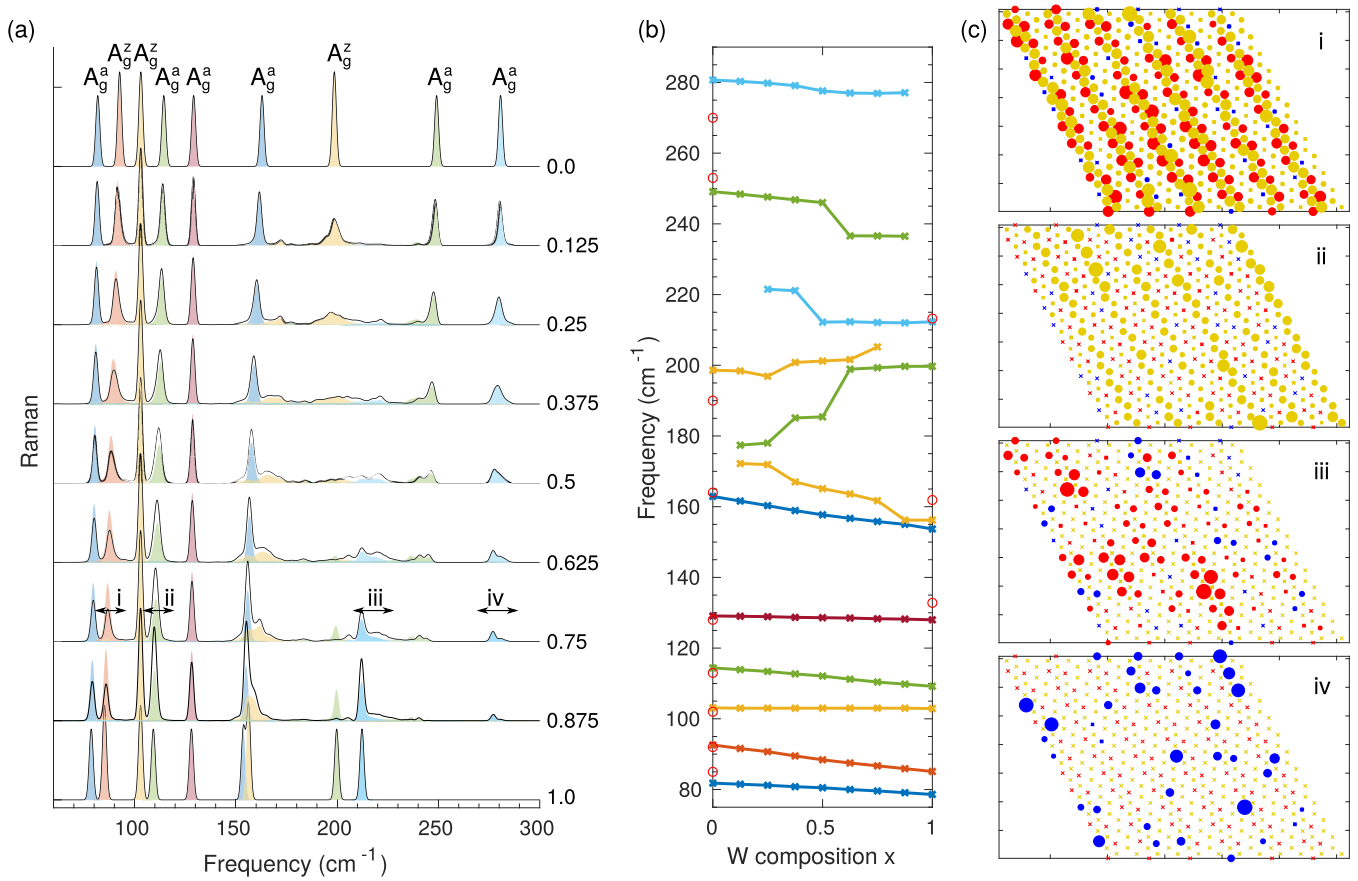

FIG. 5. (a) RGDOS for T'-(Mo,W)Te_2. The total RGDOS is shown with a solid black line. The shaded areas show contributions from the projection to eigenmodes of the pristine T′-$MoTe_2$. The modes are colored sequentially (and loops once). (b) Evolution of the peak maxima positions for $Mo_{1-x}W_xTe_2$ alloys. Experimental data (red open circles) are taken from Refs. [57,58]. (c) Illustration of selected SC eigenmodes from the $x = 0.75$ case, as indicated in (a). The SC eigenmodes within the frequency range are weighted by the projection to the dominant PC eigenmode. The blue, red, and yellow symbols correspond to Mo, W, and Te atoms, respectively.

WTe_2. For the low-frequency modes in $MoTe_2$ and WTe_2, calculated and experimental frequencies agree very well. The agreement deteriorates for high-frequency modes, but the experimental and calculated peaks can still be mapped. Also, the ordering of the A_g^a and A_g^z modes is correctly reproduced. When comparing to the bulk alloy results, our calculations indicate that the reported disorder-activated modes around 180 and 202 cm^{-1} [35] can be a mix of the last three high-frequency modes and can be tuned by varying composition. Our calculations produce a large number of small peaks at these frequencies with contributions from all three high-frequency modes, but we do not obtain one or two prominent peaks. This might be caused by normalization of Raman tensors in our simulated spectra. The peak at 130 cm^{-1} in $MoTe_2$ was found to split into two peaks separated by about 3 cm^{-1} upon increasing the W concentration [35,36] and was assigned to mixing in Ref. [35] and to a phase change from monoclinic to orthorhombic lattice in Refs. [36,61]. Since this peak is silent in the metal sublattice, it shows no alloying-induced splitting nor even any broadening in our calculations, and thus our calculations do not support the assignment to mixing. For the highest-frequency mode, our calculations correctly capture the broadening toward higher frequencies on both the $MoTe_2$ and the WTe_2 regions [35].

C. Impurities in H-MoS_2

The Raman signatures can be used to identify impurities at small concentrations (small with respect to alloying, i.e., within few percent). In some instances, as seen also in the previous sections, impurities can produce very distinct new peaks, broaden existing peaks, or result in very broad features. In this section, we insert a small number of impurity atoms into the lattice and examine the trends in the changes in the Raman spectra. The mass approximation limits our study to cases where chemical bonding upon substitution is expected to remain fairly similar. To this end, we either replace the Mo atom by another transition metal element or the S atom by an atom from the nitrogen, oxygen, or fluorine groups. Clearly, this is expected to work best for the elements in the same column in the periodic table and worsen the further away from it. The small impurity concentration helps to avoid problems with the large strain. For the calculations, we here adopt a slightly simplified procedure where we simply take the 5×5 supercell with a single impurity. This is sufficiently large to describe the localized modes, and although the peak broadenings would not be correctly described, there are very little changes in the position and broadening of the main peaks in these dilute cases.

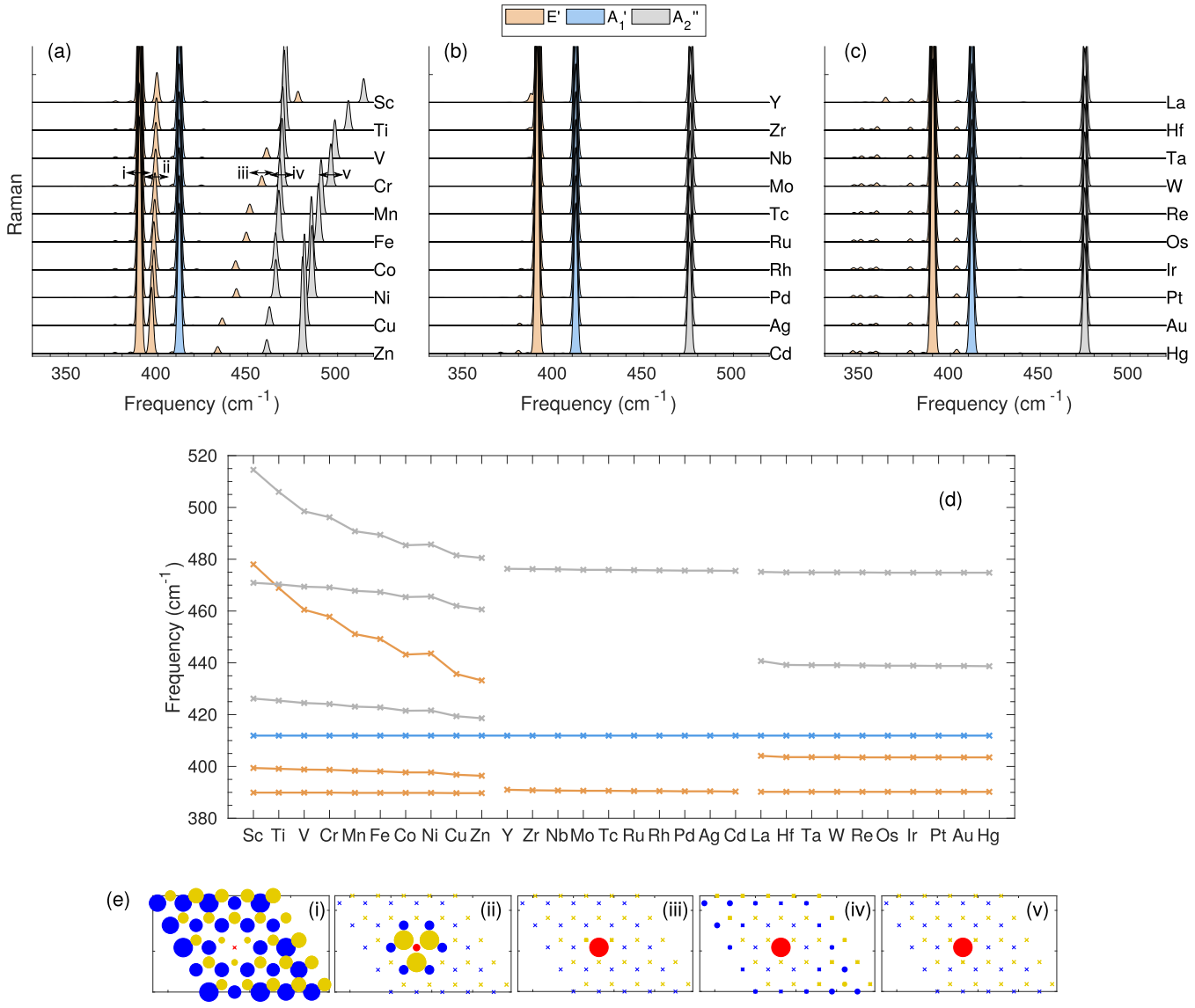

FIG. 6. (a)–(c) RGDOS for impurities in the Mo site in MoS_2, grouped by the rows in the periodic table. (d) Positions of the peak maxima extracted from panels (a)–(c). (e) Selected eigenmodes from the Cr case. The blue, red, and yellow symbols correspond to Mo, Cr, and S atoms, respectively.

The RGDOS for the Mo-site impurities are shown in Figs. 6(a)–6(c). One impurity in 25 lattice sites corresponds to the 4% impurity concentration. The behavior is clearly different for $3d$, $4d$, and $5d$ transitional metal impurities. Following the impurity masses, the additional impurity induced peaks are at highest frequencies for the $3d$ elements and at lowest frequencies for $5d$ elements, whereas the $4d$ impurities show very little new features. In case of the $3d$ elements, there is a pronounced splitting between the E' and the A_2'' modes and an additional, mostly E'-derived, mode between the two. We note again that the A_2'' mode is not Raman active and only shown here for reference. Selected eigenmodes from the Cr case are shown in Fig. 6(e). Not surprisingly, the main peak is localized in the MoS_2 regions [panel (i)]. The second E' feature is localized around the impurity [panel (ii)], and the last one is localized strictly at the impurity [panel (iii)]. This last E' peak should have appreciable Raman intensity and frequency that sensitively depends on the transition metal impurity and thus seems to provide the most effective impurity signature. For the two A_2''-derived peaks, the lower-frequency mode is localized in the MoS_2 regions [panel (iv), the Cr atom shows large weight due to its small mass, but all Mo atoms are also active] and the higher frequency one around the impurity [panel (v)].

Very little happens with the $4d$ impurities, only a small shift of the main E' mode together with slight broadening, stemming from the small (relative) change in the mass. All the $5d$ impurities show features similar to the (Mo,W)S_2 alloy considered previously: a broad set of weak features at 300–400 cm^{-1} and one peak between E' and A_1' peaks. For the two eigenmodes shown in Fig. 3(d) [panels (v) and (vi)], despite having clearly different frequencies, they have fairly similar eigenvectors. Since the MoS_2 E'', A_1, and A_2'' modes at the K and M points largely fall at frequencies between 350 and 400 cm^{-1}, we think these impurity modes have large contributions from the off-Γ k points and only a small Γ point

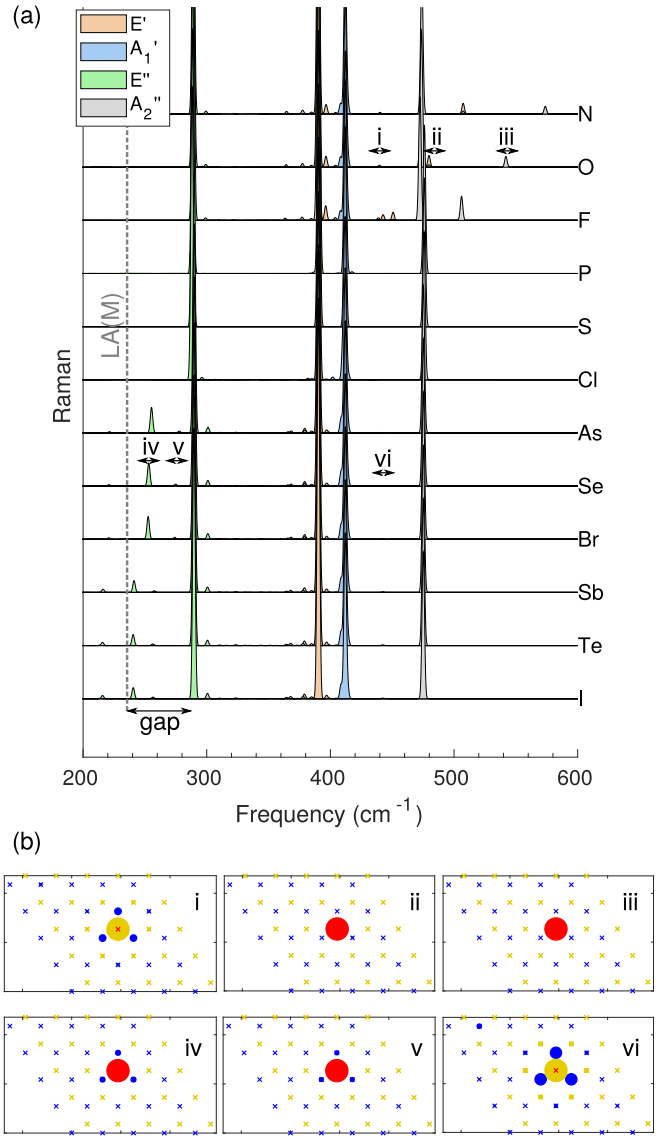

FIG. 7. (a) RGDOS for impurities in the S site in MoS_2. The LA(M) frequency from pristine MoS_2 and the gap in the phonon structure are also indicated. (b) Selected eigenmodes for the O and Se impurity systems. The blue, red, and yellow symbols correspond to Mo, O/Se, and S atoms, respectively.

Raman-active contribution. In essence, these impurities lead to mixing of the vibrational modes at different q points of the primitive cell BZ. No pronounced features are observed at low frequencies, and there are no gap states.

Overall, it appears that it should be possible to resolve the presence of even fairly dilute concentration of $3d$ transition metal impurities in MoS_2 from the splitting of the E' peak, possibly even with the elemental precision, although the absolute values given here may suffer from the limitations of the mass approximation. Dilute concentration of $4d$ impurities are expected to be largely invisible in the Raman spectra, whereas $5d$ impurities might show up in the Raman spectra, but their identification can be difficult.

The RGDOS for the S-site impurities in MoS_2 are shown in Fig. 7(a). One impurity in 50 lattice sites corresponds to 2 % impurity concentration. Again, lighter impurities lead to additional peaks at higher frequencies and heavier impurities at lower frequencies, but the features that are most likely to be observed in experiments are those falling above the A_2'' mode or inside the gap between the E'' mode and the LA(M) edge. In fact, such features have been reported in the literature for MoS_2 with light Se alloying at about 270 cm^{-1} [9,10,31,67] and with light Te alloying at about 243 cm^{-1} [68], agreeing well with our calculations.

O and Se impurities in MoS_2 are chosen as representative examples to be discussed in more detail. Selected eigenvectors of these impurity systems are presented in Fig. 7(b). In the case of the O impurity, the feature (ii) just above A_2'' is mainly derived from E' with a small E'' contribution, and it should thus be visible in Raman measurements. The high-frequency feature (iii) is mostly of A_2'' type, but it contains also an appreciable A_1' contribution and thus could also be visible. In the case of the Se impurity, there are two features in the gap with the lower one (iv) derived mostly out of E'' with some E', and the higher one (v) derived mostly from the pristine A_1' mode with some A_2'' character. Finally, we mention the features (i) and (vi), which are localized mostly at the S atom on the opposite side of the layer from the impurity atom, and thus they also have the same frequency, independent of the impurity element. Although this feature is barely visible in the simulated spectrum, it is derived mostly from the pristine A_1' mode and thus could be observable.

IV. CONCLUSIONS

We have devised an efficient computational method to simulate Raman spectra of large systems, being especially applicable to alloys and systems with small numbers of defects. The method is based on the projection of vibrational eigenvectors of the supercell to the eigenvectors from the primitive cell and using them as weights in summing over the Raman tensors calculated at the primitive cell. We moreover used mass approximation to rapidly evaluate the vibrational modes in the supercell. We applied the method to two different transition metal dichalcogenide monolayer alloys H-(Mo,W)S_2 and T′-(Mo,W)Te_2 and to impurities in H-MoS_2. The accuracy of the method was validated in the case of the H-(Mo,W)S_2 alloy through comparison to the available experimental reports. T′-(Mo,W)Te_2 and impurity cases are used to: (i) demonstrate the wider applicability of the method and (ii) provide predictions in few technologically relevant systems. We note that, in addition to yielding the simulated Raman spectra, the projection scheme also provides a powerful tool for analyzing the origin of the Raman-active features. The method presented here is not limited to 2D materials and is applicable to various other bulk and low-dimensional systems.

ACKNOWLEDGMENTS

We thank Professor L. Xie for providing us the experimental data. We are grateful to the Academy of Finland for support under Projects No. 286279 and No. 311058. A.V.K. further acknowledges the German Research Foundation (DFG) for support through project KR 4866/2-1. We also thank CSC–IT Center for Science Ltd. and Aalto Science-IT project for generous grants of computer time.

[1] V. Nicolosi, M. Chhowalla, M. G. Kanatzidis, M. S. Strano, and J. N. Coleman, Liquid exfoliation of layered materials, Science **340**, 1226419 (2013).

[2] S. Lebègue, T. Björkman, M. Klintenberg, R. M. Nieminen, and O. Eriksson, Two-Dimensional Materials from Data Filtering and Ab Initio Calculations, Phys. Rev. X **3**, 031002 (2013).

[3] N. Mounet, M. Gibertini, P. Schwaller, D. Campi, A. Merkys, A. Marrazzo, T. Sohier, I. E. Castelli, A. Cepellotti, G. Pizzi, and N. Marzari, Two-dimensional materials from high-throughput computational exfoliation of experimentally known compounds, Nat. Nanotechnol. **13**, 246 (2018).

[4] E. Revolinsky and D. Beerntsen, Electrical properties of the $MoTe_2$-WTe_2 and $MoSe_2$-WSe_2 systems, J. Appl. Phys. **35**, 2086 (1964).

[5] S. K. Srivastava, T. K. Mandal, and B. K. Samantaray, Studies on layer disorder, microstructural parameters and other properties of tungsten-substitued molybdenum disulfide, $Mo_{1-x}W_xS_2$ ($0 \leqslant x \leqslant 1$), Synth. Met. **90**, 135 (1997).

[6] Y. Chen, J. Xi, D. O. Dumcenco, Z. Liu, K. Suenaga, D. Wang, Z. Shuai, Y.-S. Huang, and L. Xie, Tunable band gap photoluminescence from atomically thin transition-metal dichalcogenide alloys, ACS Nano **7**, 4610 (2013).

[7] H.-P. Komsa and A. V. Krasheninnikov, Two-dimensional transition metal dichalcogenide alloys: Stability and electronic properties, J. Phys. Chem. Lett. **3**, 3652 (2012).

[8] J. Kang, S. Tongay, J. Li, and J. Wu, Monolayer semiconducting transition metal dichalcogenide alloys: Stability and band bowing, J. Appl. Phys. **113**, 143703 (2013).

[9] H. Li, X. Duan, X. Wu, X. Zhuang, H. Zhou, Q. Zhang, X. Zhu, W. Hu, P. Ren, P. Guo, L. Ma, X. Fan, X. Wang, J. Xu, A. Pan, and X. Duan, Growth of alloy $MoS_{2x}Se_{2(1-x)}$ nanosheets with fully tunable chemical compositions and optical properties, J. Am. Chem. Soc. **136**, 3756 (2014).

[10] J. Mann, Q. Ma, P. M. Odenthal, M. Isarraraz, D. Le, E. Preciado, D. Barroso, K. Yamaguchi, G. von Son Palacio, A. Nguyen, T. Tran, M. Wurch, A. Nguyen, V. Klee, S. Bobek, D. Sun, T. F. Heinz, T. S. Rahman, R. Kawakami, and L. Bartels, 2-Dimensional transition metal dichalcogenides with tunable direct band gaps: $MoS_{2(1-x)}Se_{2x}$ monolayers, Adv. Mater. **26**, 1399 (2014).

[11] A. F. Rigosi, H. M. Hill, K. T. Rim, G. W. Flynn, and T. F. Heinz, Electronic band gaps and exciton binding energies in monolayer $Mo_xW_{1-x}S_2$ transition metal dichalcogenide alloys probed by scanning tunneling and optical spectroscopy, Phys. Rev. B **94**, 075440 (2016).

[12] G. Wang, C. Robert, A. Suslu, B. Chen, S. Yang, S. Alamdari, I. C. Gerber, T. Amand, X. Marie, S. Tongay, and B. Urbaszek, Spin-orbit engineering in transition metal dichalcogenide alloy monolayers, Nat. Commun. **6**, 10110 (2015).

[13] X. Gu and R. Yang, Phonon transport in single-layer $Mo_{1-x}W_xS_2$ alloy embedded with WS_2 nanodomains, Phys. Rev. B **94**, 075308 (2016).

[14] X. Qian, P. Jiang, P. Yu, X. Gu, Z. Liu, and R. Yang, Anisotropic thermal transport in van der waals layered alloys $WSe_{2(1-x)}Te_{2x}$, Appl. Phys. Lett. **112**, 241901 (2018).

[15] B. Huang, M. Yoon, B. G. Sumpter, S.-H. Wei, and F. Liu, Alloy Engineering of Defect Properties in Semiconductors: Suppression of Deep Levels in Transition-Metal Dichalcogenides, Phys. Rev. Lett. **115**, 126806 (2015).

[16] J. Yao, Z. Zheng, and G. Yang, Promoting the performance of layered-material photodetectors by alloy engineering, ACS Appl. Mater. Interfaces **8**, 12915 (2016).

[17] V. Kiran, D. Mukherjee, R. N. Jenjeti, and S. Sampath, Active guests in the MoS_2/$MoSe_2$ host lattice: Efficient hydrogen evolution using few-layer alloys of $MoS_{2(1-x)}Se_{2x}$, Nanoscale **6**, 12856 (2014).

[18] L. Wang, Z. Sofer, J. Luxa, and M. Pumera, $Mo_xW_{1-x}S_2$ solid solutions as 3D electrodes for hydrogen evolution reaction, Adv. Mater. Interfaces **2**, 1500041 (2015).

[19] M. A. Cazalilla, H. Ochoa, and F. Guinea, Quantum Spin Hall Effect in Two-Dimensional Crystals of Transition-Metal Dichalcogenides, Phys. Rev. Lett. **113**, 077201 (2014).

[20] X. Qian, J. Liu, L. Fu, and J. Li, Quantum spin hall effect in two-dimensional transition metal dichalcogenides, Science **346**, 1344 (2014).

[21] Y. Sun, S.-C. Wu, M. N. Ali, C. Felser, and B. Yan, Prediction of weyl semimetal in orthorhombic $MoTe_2$, Phys. Rev. B **92**, 161107 (2015).

[22] L. Huang, T. M. McCormick, M. Ochi, Z. Zhao, M.-T. Suzuki, R Arita, Y. Wu, D. Mou, H. Cao, J. Yan, N. Trivedi, and A. Kaminski, Spectroscopic evidence for a type II weyl semimetallic state in $MoTe_2$, Nature Mater. **15**, 1155 (2016).

[23] K.-A. N. Duerloo and E. J. Reed, Structural phase transitions by design in monolayer alloys, ACS Nano **10**, 289 (2016).

[24] C. Zhang, S. KC, Y. Nie, C. Liang, W. G. Vandenberghe, R. C. Longo, Y. Zheng, F. Kong, S. Hong, R. M. Wallace, and K. Cho, Charge mediated reversible metal-insulator transition in monolayer $MoTe_2$ and $W_xMo_{1-x}Te_2$ alloy, ACS Nano **10**, 7370 (2016).

[25] Z. Fei, W. Zhao, T. A. Palomaki, B. Sun, M. K. Miller, Z. Zhao, J. Yan, X. Xu, and D. H. Cobden, Ferroelectric switching of a two-dimensional metal, Nature (London) **560**, 336 (2018).

[26] Y. Chen, D. O. Dumcenco, Y. Zhu, X. Zhang, N. Mao, Q. Feng, M. Zhang, J. Zhang, P.-H. Tan, Y.-S. Huang, and L. Xie, Composition-dependent raman modes of $Mo_{1-x}W_xS_2$ monolayer alloys, Nanoscale **6**, 2833 (2014).

[27] H. Liu, K. K. A. Antwi, S. Chua, and D. Chi, Vapor-phase growth and characterization of $Mo_{1-x}W_xS_2$ ($0 \leqslant x \leqslant 1$) atomic layers on 2-inch sapphire substrates, Nanoscale **6**, 624 (2014).

[28] J. Park, M. S. Kim, B. Park, S. H. Oh, S. Roy, J. Kim, and W. Choi, Composition-tunable synthesis of large-scale $Mo_{1-x}W_xS_2$ alloys with enhanced photoluminescence, ACS Nano **12**, 6301 (2018).

[29] S. Tongay, D. S. Narang, J. Kang, W. Fan, C. Ko, A. V. Luce, K. X. Wang, J. Suh, K. D. Patel, V. M. Pathak, J. Li, and J. Wu, Two-dimensional semiconductor alloys: Monolayer $Mo_{1-x}W_xSe_2$, Appl. Phys. Lett. **104**, 012101 (2014).

[30] M. Zhang, J. Wu, Y. Zhu, D. O. Dumcenco, J. Hong, N. Mao, S. Deng, Y. Chen, Y. Yang, C. Jin, S. H. Chaki, Y.-S. Huang, J. Zhang, and L. Xie, Two-dimensional molybdenum tungsten diselenide alloys: Photoluminescence, raman scattering, and electrical transport, ACS Nano **8**, 7130 (2014).

[31] Q. Feng, N. Mao, J. Wu, H. Xu, C. Wang, J. Zhang, and L. Xie, Growth of $MoS_{2(1-x)}Se_{2x}$ ($x = 0.41 - 1.00$) monolayer alloys with controlled morphology by physical vapor deposition, ACS Nano **9**, 7450 (2015).

[32] S.-H. Su, Y.-T. Hsu, Y.-H. Chang, M.-H. Chiu, C.-L. Hsu, W.-T. Hsu, W.-H. Chang, J.-H. He, and L.-J. Li, Band gap-tunable

molybdenum sulfide selenide monolayer alloy, Small **10**, 2589 (2014).

[33] W. Wen, Y. Zhu, X. Liu, H.-P. Hsu, Z. Fei, Y. Chen, X. Wang, M. Zhang, K.-H. Lin, F.-S. Huang, Y.-P. Wang, Y.-S. Huang, C.-H. Ho, P.-H. Tan, C. Jin, and L. Xie, Anisotropic spectroscopy and electrical properties of 2D $ReS_{2(1-x)}Se_{2x}$ alloys with distorted 1T structure, Small **13**, 1603788 (2017).

[34] D. O. Dumcenco, K. Y. Chen, Y. P. Wang, Y. S. Huang, and K. K. Tiong, Raman study of 2H-$Mo_{1-x}W_xS_2$ layered mixed crystals, J. Alloys Compd. **506**, 940 (2010).

[35] S. M. Oliver, R. Beams, S. Krylyuk, I. Kalish, A. K Singh, A. Bruma, F. Tavazza, J. Joshi, I. R. Stone, S. J. Stranick, A. V. Davydov, and P. M. Vora, The structural phases and vibrational properties of $Mo_{1-x}W_xTe_2$ alloys, 2D Mater. **4**, 045008 (2017).

[36] Y.-Y. Lv, L. Cao, X. Li, B.-B. Zhang, K. Wang, B. Pang, L. Ma, D. Lin, S.-H. Yao, J. Zhou, Y. B. Chen, S.-T. Dong, W. Liu, M.-H. Lu, Y. Chen, and Y.-F. Chen, Composition and temperature-dependent phase transition in miscible $Mo_{1-x}W_xTe_2$ single crystals, Sci. Rep. **7**, 44587 (2017).

[37] A. Molina-Sánchez and L. Wirtz, Phonons in single-layer and few-layer MoS_2 and WS_2, Phys. Rev. B **84**, 155413 (2011).

[38] X. Zhang, X.-F. Qiao, W. Shi, J.-B. Wu, D.-S. Jiang, and P.-H. Tan, Phonon and raman scattering of two-dimensional transition metal dichalcogenides from monolayer, multilayer to bulk material, Chem. Soc. Rev. **44**, 2757 (2015).

[39] R. Saito, Y. Tatsumi, S. Huang, X. Ling, and M. S. Dresselhaus, Raman spectroscopy of transition metal dichalcogenides, J. Phys.: Condens. Matter **28**, 353002 (2016).

[40] W. M. Parkin, A. Balan, L. Liang, P. M. Das, M. Lamparski, C. H. Naylor, J. A. Rodríguez-Manzo, A. T. C. Johnson, V. Meunier, and M. Drndić, Raman shifts in electron-irradiated monolayer MoS_2, ACS Nano **10**, 4134 (2016).

[41] S. Bae, N. Sugiyama, T. Matsuo, H. Raebiger, K.-I. Shudo, and K. Ohno, Defect-Induced Vibration Modes of Ar^+-Irradiated MoS_2, Phys. Rev. Appl. **7**, 024001 (2017).

[42] S. Baroni, S. de Gironcoli, and P. Giannozzi, Phonon Dispersions in $Ga_xAl_{(1-x)}$ As Alloys, Phys. Rev. Lett. **65**, 84 (1990).

[43] J. Menéndez, Characterization of bulk semiconductors using raman spectroscopy, in *Raman Scattering in Materials Science*, edited by W. H. Weber and R. Merlin (Springer, Berlin/Heidelberg, 2000), pp. 55–103.

[44] P. B. Allen, T. Berlijn, D. A. Casavant, and J. M. Soler, Recovering hidden bloch character: Unfolding electrons, phonons, and slabs, Phys. Rev. B **87**, 085322 (2013).

[45] F. Zheng and P. Zhang, Phonon dispersion unfolding in the presence of heavy breaking of spatial translational symmetry, Comput. Mater. Sci. **125**, 218 (2016).

[46] H. Huang, F. Zheng, P. Zhang, J. Wu, B.-L. Gu, and W. Duan, A general group theoretical method to unfold band structures and its application, New J. Phys. **16**, 033034 (2014).

[47] A. B. Gordienko, K. A. Gordienko, and A. V. Kopytov, Unfolding phonon spectra by smearing of vibrational eigenmodes, Phys. Status Solidi B **254**, 1700213 (2017).

[48] Y. Ikeda, A. Carreras, A. Seko, A. Togo, and I. Tanaka, Mode decomposition based on crystallographic symmetry in the band-unfolding method, Phys. Rev. B **95**, 024305 (2017).

[49] Q. Qian, Z. Zhang, and K. J. Chen, In situ resonant raman spectroscopy to monitor the surface functionalization of MoS_2WSe_2 for high-k integration: A first-principles study, Langmuir **34**, 2882 (2018).

[50] G. Kresse and J. Hafner, Ab initio molecular dynamics for liquid metals, Phys. Rev. B **47**, 558 (1993).

[51] J. P. Perdew, A. Ruzsinszky, G. I. Csonka, O. A. Vydrov, G. E. Scuseria, L. A. Constantin, X. Zhou, and K. Burke, Restoring the Density-Gradient Expansion for Exchange in Solids and Surfaces, Phys. Rev. Lett. **100**, 136406 (2008).

[52] D. Porezag and M. R. Pederson, Infrared intensities and raman-scattering activities within density-functional theory, Phys. Rev. B **54**, 7830 (1996).

[53] A. Togo and I. Tanaka, First principles phonon calculations in materials science, Scr. Mater. **108**, 1 (2015).

[54] Tsachi Livneh and Jonathan E Spanier, A comprehensive multi-phonon spectral analysis in MoS_2, 2D Mater. **2**, 035003 (2015).

[55] A. Zunger, S.-H. Wei, L. G. Ferreira, and James E. Bernard, Special Quasirandom Structures, Phys. Rev. Lett. **65**, 353 (1990).

[56] J. Joshi, I. R. Stone, R. Beams, S. Krylyuk, I. Kalish, A. V. Davydov, and P. M. Vora, Phonon anharmonicity in bulk Td-$MoTe_2$, Appl. Phys. Lett. **109**, 031903 (2016).

[57] Y. C. Jiang, J. Gao, and L. Wang, Raman fingerprint for semi-metal WTe_2 evolving from bulk to monolayer, Sci. Rep. **6**, 19624 (2016).

[58] S.-Y. Chen, C. H. Naylor, T. Goldstein, A. T. C. Johnson, and J. Yan, Intrinsic phonon bands in high-quality monolayer T' molybdenum ditelluride, ACS Nano **11**, 814 (2017).

[59] Y. Kim, Y. I. Jhon, J. Park, J. H. Kim, S. Lee, and Y. M. Jhon, Anomalous raman scattering and lattice dynamics in mono- and few-layer WTe_2, Nanoscale **8**, 2309 (2016).

[60] R. Beams, L. Gustavo Cançado, S. Krylyuk, I. Kalish, B. Kalanyan, A. K. Singh, K. Choudhary, A. Bruma, P. M. Vora, F. Tavazza, A. V. Davydov, and S. J. Stranick, Characterization of few-layer 1T′ $MoTe_2$ by polarization-resolved second harmonic generation and raman scattering, ACS Nano **10**, 9626 (2016).

[61] S.-Y. Chen, T. Goldstein, D. Venkataraman, A. Ramasubramaniam, and J. Yan, Activation of new raman modes by inversion symmetry breaking in type II weyl semimetal candidate T′-$MoTe_2$, Nano Lett. **16**, 5852 (2016).

[62] M. Grzeszczyk, K. Gołasa, M. Zinkiewicz, K. Nogajewski, M. R. Molas, M. Potemski, A. Wysmołek, and A. Babiński, Raman scattering of few-layers $MoTe_2$, 2D Mater. **3**, 025010 (2016).

[63] K. Zhang, C. Bao, Q. Gu, X. Ren, H. Zhang, K. Deng, Y. Wu, Y. Li, J. Feng, and S. Zhou, Raman signatures of inversion symmetry breaking and structural phase transition in type-II Weyl semimetal $MoTe_2$, Nat. Commun. **7**, 13552 (2016).

[64] J. Wang, X. Luo, S. Li, I. Verzhbitskiy, W. Zhao, S. Wang, S. Y. Quek, and G. Eda, Determination of crystal axes in semimetallic T'-$MoTe_2$ by polarized raman spectroscopy, Adv. Funct. Mater. **27**, 1604799 (2017).

[65] D. Rhodes, D. A. Chenet, B. E. Janicek, C. Nyby, Y. Lin, W. Jin, D. Edelberg, E. Mannebach, N. Finney, A. Antony, T. Schiros, T. Klarr, A. Mazzoni, M. Chin, Y.-c Chiu, W. Zheng, Q. R. Zhang, F. Ernst, J. I. Dadap, X. Tong, J. Ma, R. Lou, S. Wang, T. Qian, H. Ding, R. M. Osgood, D. W. Paley, A. M. Lindenberg, P. Y. Huang, A. N. Pasupathy, M. Dubey, J. Hone, and L. Balicas, Engineering the structural and electronic phases of $MoTe_2$ through W substitution, Nano Lett. **17**, 1616 (2017).

[66] X. Ma, P. Guo, C. Yi, Q. Yu, A. Zhang, J. Ji, Y. Tian, F. Jin, Y. Wang, K. Liu, T. Xia, Y. Shi, and Q. Zhang, Raman scattering in the transition-metal dichalcogenides of 1T′-$MoTe_2$,T_d -$MoTe_2$, and T_d-WTe_2, Phys. Rev. B **94**, 214105 (2016).

[67] S.-H. Su, W.-T. Hsu, C.-L. Hsu, C.-H. Chen, M.-H. Chiu, Y.-C. Lin, W.-H. Chang, K. Suenaga, J.-H. He, and L.-J. Li, Controllable synthesis of band-gap-tunable and monolayer transition-metal dichalcogenide alloys, Frontiers in Energy Research **2**, 27 (2014).

[68] G. Yin, D. Zhu, D. Lv, A. Hashemi, Z. Fei, F. Lin, A. V. Krasheninnikov, Z. Zhang, H.-P. Komsa, and C. Jin, Hydrogen-assisted post-growth substitution of tellurium into molybdenum disulfide monolayers with tunable compositions, Nanotechnology **29**, 145603 (2018).